ACS Energy LETTERS

http://pubs.acs.org/journal/aelccp

Enhanced Redox Storage and Diverse Intercalation in Layered Metal Organic Frameworks with a Staggered Stacking Mode

Satya Prakash Suman, Gopi M. R. Dontireddy, Tianyang Chen, Jiande Wang, Jin-Hu Dou, and Harish Banda*

Cite This: *ACS Energy Lett.* 2024, 9, 1572−1580

Read Online

ACCESS | Metrics & More | Article Recommendations | Supporting Information

ABSTRACT: Two-dimensional metal organic frameworks (2D MOFs) with honeycomb-like porous sheets are of growing interest for applications in electrochemical energy storage and electrocatalysis. Notably, 2D MOFs that host their porous sheets in eclipsed or slipped-parallel stacking modes possess continuous one-dimensional pores (1D) and have been widely studied. In contrast, related 2D MOFs with a staggered stacking mode have reduced porosity, are relatively rare, and are largely unexplored for applications. Here we report 2-fold enhanced redox storage and intercalation of diverse ions in a staggered-stacked, nonporous 2D MOF over its eclipsed-stacked, porous counterpart. Interestingly, both MOFs, despite undergoing similar ligand-centered redox processes, differ by storing four and two electrons per formula unit of the staggered and eclipsed phases, respectively. Taken together, the stacking mode-dependent modulation of a ligand's redox behavior in 2D MOFs offers a new avenue to tune structure−property relationships and presents important motivation to explore nonporous 2D MOFs.

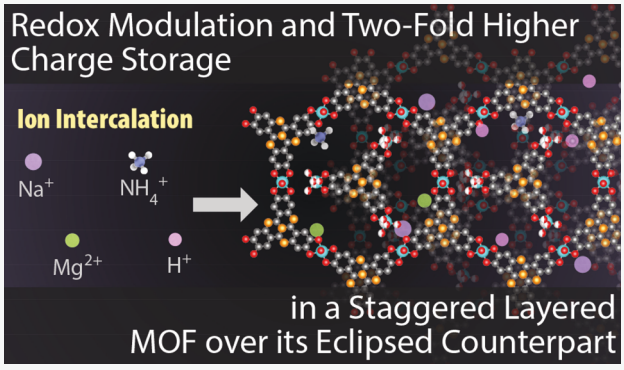

Two-dimensional, π-conjugated layered metal organic frameworks (2D MOFs) offer a unique combination of porosity and electronic delocalization in extended crystal lattices and have demonstrated great potential as electrocatalysts and electrodes for electrochemical energy storage.[1−4] Typically, metal ions favoring a square-planar coordination mode bond strongly with multitopic, planar aromatic linkers and create porous 2D sheets. These sheets interact through out-of-plane $\pi-\pi$ interactions and stack in eclipsed, slipped-parallel, or staggered fashion. Eclipse and slip-stacked modes create open one-dimensional (1D) pores that are explored as highly advantageous for rapid ion transport and sorption.[5,6] For instance, electrochemical capacitors using 2D MOFs based on 2,3,6,7,10,11-hexaiminotriphenylene (HITP),[7−9] 2,3,6,7,10,11-hexahydroxytriphenylene (HHTP),[10−12] hexaaminobenzene (HAB),[13−15] and phthalocyanine[16,17] deliver greater capacitances than activated carbons. On the other hand, staggered mode reduces or, in some cases, eliminates porosity, rendering such 2D MOFs as nonporous and less attractive for capacitive charge storage.[18,19] Notably, these nonporous MOFs, which are similar to other 2D van der Waals materials[20−23] in their layered structures, offer a possibility for intercalation-based enhanced charge storage.[24−26] Moreover, an observation of intercalation in these nonporous MOFs can enable synthesis of unique intercalation compounds with honeycomb-like lattices, opening frontiers for evaluation of electronic properties in intercalation compounds beyond those based on graphite and transition-metal dichaclogenides.[27,28] However, because staggering causes partial loss of $\pi-\pi$ interactions, 2D MOFs with such a stacking mode are uncommon, and investigations into their electrochemical behavior are rare.

Axial positions strongly influence the overall stacking mode when 2D MOFs host six-coordinate octahedral metal ions instead of four-coordinate square-planar ions. These positions, typically occupied by coordinating solvent molecules, potentially disrupt out-of-plane $\pi-\pi$ interactions, counter the expected relative stabilities of the three stacking modes, and

Received: February 22, 2024
Accepted: March 13, 2024
Published: March 18, 2024

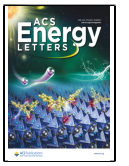

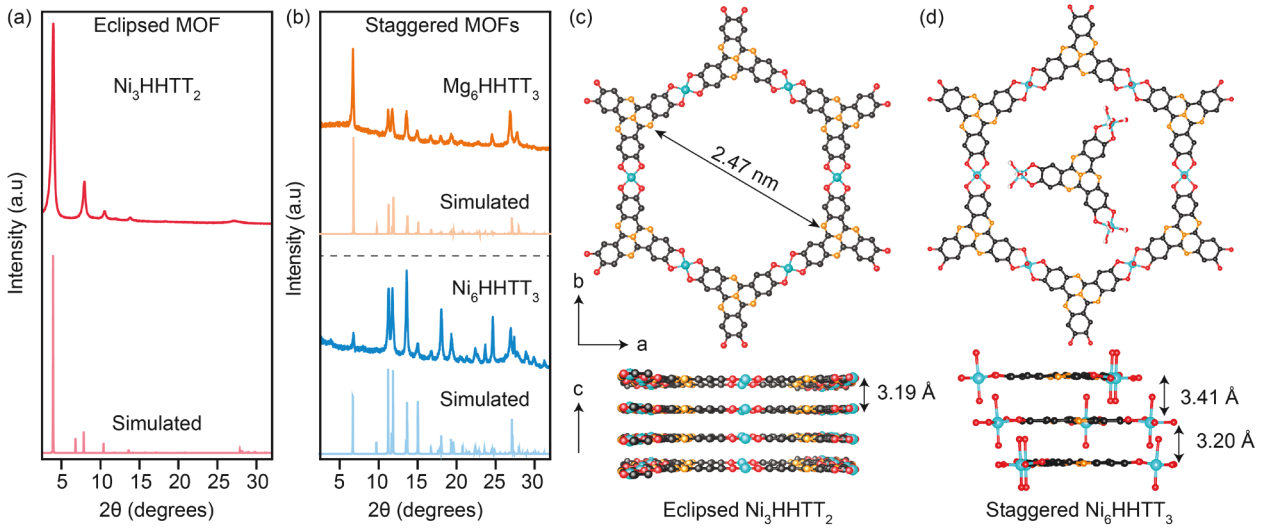

Figure 1. X-ray diffraction patterns of the (a) eclipsed Ni_3HHTT_2 and (b) staggered MOFs Ni_6HHTT_3 and Mg_6HHTT_3. Crystal structures of (c) eclipsed Ni_3HHTT_2 and (d) staggered Ni_6HHTT_3 shown in the *ab* plane and along the *c* axis. While Ni_3HHTT_2 has a 1D open pore, Ni_6HHTT_3 has staggered packing and trinuclear guest complexes in its in-plane pores, which, together, eliminate porosity. Mg_6HHTT_3, not shown here, has a similar structure as Ni_6HHTT_3.

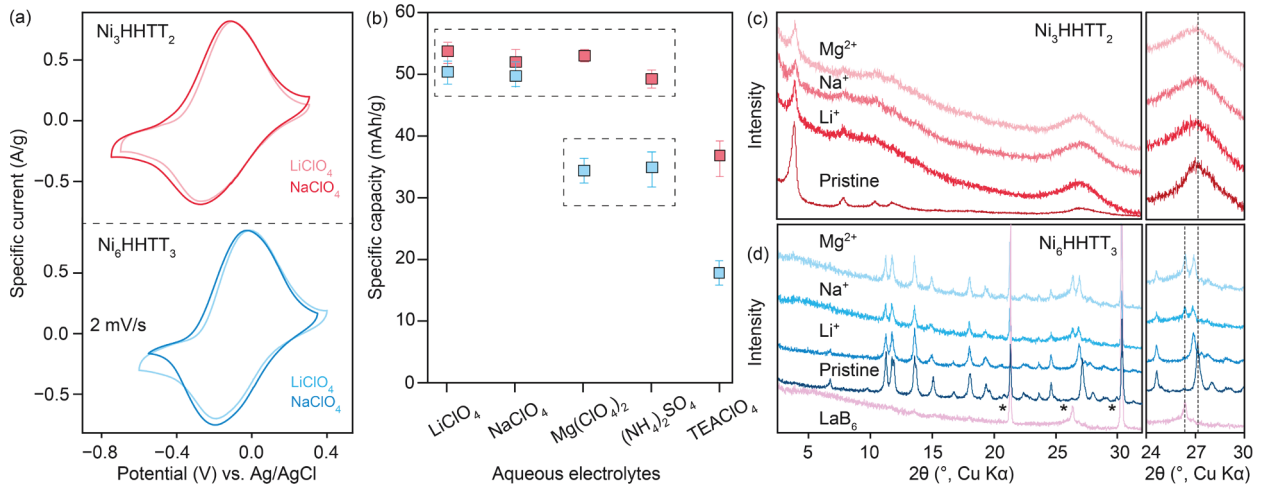

Figure 2. (a) Cyclic voltammetry curves of Ni_3HHTT_2 and Ni_6HHTT_3 recorded at a scan rate of 2 mV/s in aqueous 0.5 M $LiClO_4$ and $NaClO_4$ electrolytes. (b) Specific discharge capacities of the two Ni-MOFs in a variety of aqueous electrolytes −0.5 M $LiClO_4$, $NaClO_4$, $Mg(ClO_4)_2$, $(NH_4)_2SO_4$, and $TEAClO_4$ at a slow scan rate of 0.2 mV/s. Capacities and error bars are obtained from the average of data from different electrodes (Tables S1 & S2). (c) Ex situ powder X-ray diffraction patterns for pristine and negatively polarized electrodes (−0.5 V vs Ag/AgCl) of both Ni-MOFs in various aqueous electrolytes. Black lines are added as guides for the reader. Lanthanum boride (LaB_6) is added as an internal standard to Ni_6HHTT_3.

deliver unique crystal structures. Indeed, the first report on 2D MOFs, catecholate-based $Co_6HHTP_3{\cdot}18H_2O$ by Yaghi et. al,[29] has octahedral Co^{2+} ions that occupy two crystallographically independent positions—one in the honeycomb layer and the other in a layer of discrete trinuclear complexes. Recently, Dincă et al. reported multiple 2D MOFs with metal nodes in octahedral coordination geometries using 2,3,7,8,12,13-hexahydroxytetraazanaphthotetraphene (HHTT) ligand.[19] Here again, the octahedral metal ions occupy two independent positions. However, unlike Co_6HHTP_3, the honeycomb sheets are arranged in a staggered fashion and the trinuclear complexes occupy hexagonal pores, rendering MOFs as completely nonporous. Overall, this unique family of staggered MOFs presents multiple candidates that offer a distinct opportunity to probe electrochemical behavior, and the possibility of intercalation, in nonporous 2D MOFs.

Here we report intercalation-based charge storage and a strong modulation of redox properties between staggered and eclipsed 2D MOFs. Specifically, we explore the ability of Ni^{2+} ions to exist in square planar and octahedral coordination environments with HHTT and study two comparable MOFs—Ni_3HHTT_2, which is eclipsed and porous, versus Ni_6HHTT_3, which is staggered and nonporous. The eclipsed phase undergoes a two-electron, ligand-centered redox process with ion sorption in its pores, whereas the staggered phase undergoes a four-electron redox event with intercalation of ions. Control studies using Mg_6HHTT_3, an analogous staggered MOF, also displays an intercalation-based, four-electron, ligand-centered redox process, confirming the overall modulation in redox properties based on the stacking mode.

Eclipsed and staggered phases of HHTT-based Ni-MOFs were synthesized according to reported procedures (details in

https://doi.org/10.1021/acsenergylett.4c00544
ACS Energy Lett. 2024, 9, 1572−1580

experimental methods, Schemes S1−S3 & Figure S1).[19] Powder X-ray diffraction patterns of obtained materials confirmed the purity of both phases (Figure 1a,b). The eclipsed phase has a formula unit of Ni_3HHTT_2, where Ni^{2+} ions bond to two neighboring $HHTT^{3-}$ cores and form a square-planar $[NiO_4]$ secondary building unit, leading to planar sheets. The resulting honeycomb-like sheets stack in an eclipsed AA fashion with a short interlayer spacing of 3.19 Å and create 1D pores with a diameter of 2.47 nm that give a N_2 sorption-based specific surface area (SSA) of 1110 ± 11 m^2/g (Figure 1c).[19] On the other hand, the staggered phase hosts Ni^{2+} ions in an octahedral coordination geometry in two crystallographically independent positions—one in honeycomb-like 2D sheets and the other in trinickel clusters (Figure 1d). The 2D sheets were formed by Ni^{2+} and $HHTT^{3-}$ in the same manner as Ni_3HHTT_2, except that two water molecules bond to the axial positions of Ni^{2+}, giving a formula of $Ni_3HHTT_2(H_2O)_6$. The presence of axial water disrupts π-stacking, increases interlayer spacing to 3.2−3.4 Å, and causes slippage of 2D sheets into a staggered ABC packing motif.[19] The staggered packing eliminates 1D pores, and the remaining open space within each 2D sheet is occupied by $[Ni(H_2O)_4]_3(HHTT)$ clusters, wherein HHTT is assigned to be in −6 state.[19] Overall, the staggered phase has a formula of $[[Ni(H_2O)_4]_3(HHTT)\cdot Ni_3(HHTT)_2(H_2O)_6]$ and a low SSA of 25 ± 11 m^2/g. An analogous 2D MOF with Mg^{2+} nodes also adapts a staggered, nonporous structure with a similar formula, serving as an ideal control material for our studies. Both staggered MOFs are hereafter referred to as M_6HHTT_3 (M = Ni/Mg). All three MOFs studied in this work have rod-like morphologies with sizes ranging from hundreds of nanometers to a few micrometers (Figure S2).

Intercalation in Staggered Ni_6HHTT_3. The electrochemical charge storage behavior of Ni_3HHTT_2 and Ni_6HHTT_3 was first studied in aqueous electrolytes by using perchlorate salts of alkali metals. Working electrodes were prepared by directly pressing pristine MOF powders on nickel foam substrates, and electrochemical tests were conducted in custom-built Swagelok-type three-electrode cells using Ag/AgCl and large activated carbon films as reference and counter electrodes, respectively (details in experimental methods). Cyclic voltammograms (CVs) recorded at a scan rate of 2 mV/s in 0.5 M $LiClO_4$ and $NaClO_4$ under reductive potential windows between −0.6 to 0.4 V vs Ag/AgCl (Figure 2a) display one set of reversible redox peaks in both MOFs. Both materials deliver specific charge storage capacities of ∼50 mAh/g at a slow scan rate of 0.2 mV/s (Figure 2b, Tables S1 & S2). The similarities in CVs and capacities, despite the significant differences in porosity noted between the two MOFs (*vide supra*), can be explained either through an outer surface-based adsorption mechanism in both MOFs or by suggesting different ion sorption mechanism in each MOF.[24]

Studies using a variety of electrolytic ion sizes are typically used to evaluate the possibility of outer surface-based adsorption processes.[15,30−34] For instance, a prior study found that 2D MOFs undergoing outer surface-based ion sorption deliver similar charge storage capacities in a variety of electrolytes, including smaller ions like Li^+ and Na^+, as well as larger organic cations such as tetrabutylammonium (TBA^+) and tetrahexylammonium (THA^+).[15] In our case, studies in electrolytes beyond $LiClO_4$ and $NaClO_4$ showed distinct charge storage behaviors in both MOFs (Figures 2b & S3−S5). Ni_6HHTT_3 showed a strong decrease in its capacities from Li^+- and Na^+-based electrolytes to divalent Mg^{2+}-, multi atomic ammonium (NH_4^+)-, and to larger tetraethylammonium cation (TEA^+)-based electrolytes. Ni_3HHTT_2 displayed similar capacities as Li^+ and Na^+ in both Mg^{2+} and NH_4^+ electrolytes, but it also showed slightly lower capacities with TEA^+, which has a solvated ion size within the range of the 1D pore size in Ni_3HHTT_2. These cation-size-dependent charge capacities rule out a surface-based charge-storage mechanism in both MOFs. Additionally, between the two MOFs, Ni_6HHTT_3 differs from Ni_3HHTT_2 by delivering lower capacities in $Mg(ClO_4)_2$, $(NH_4)_2SO_4$, and $TEAClO_4$ electrolytes. Taken together, whereas the behavior of porous Ni_3HHTT_2 may be explained by ion sorption in its 1D pores (∼2.3 nm), lower capacities noted for Ni_6HHTT_3 in tests using larger cations suggest, in the absence of a pore-based sieving,[35] a possibility of intercalation-based ion sorption mechanism.

The possibility of different ion sorption mechanisms between the MOFs and intercalation in staggered Ni_6HHTT_3 is investigated through *ex situ* powder X-ray diffraction (PXRD) studies on negatively polarized electrodes at −0.5 V vs Ag/AgCl (see experimental methods, Figures 2c, S6, & S7). PXRD patterns of negatively polarized eclipsed Ni_3HHTT_2 present diffraction patterns similar to those of the pristine material, confirming retention of crystallinity under polarization and indicating that the charge storage processes do not cause structural changes. On the other hand, polarized electrodes of staggered MOF indicate a notable shift in the [001] reflection relative to 27.06° of the pristine material (Table S3). The shift in this reflection, which is verified through an internal reference of LaB_6, confirms expansion of the lattice upon insertion of ions and the possibility of intercalation in Ni_6HHTT_3. Moreover, continuous cycling of the MOF at a slow scan rate of 2 mV/s over 72 h displays stable behavior and retention of crystallinity (Figure S8).

It is noteworthy that the increases in interlayer separation exhibit no dependence on the electrolytes and are similarly small (Figure 2c, Table S3), questioning the identity of intercalating charge-carrier ion.[36] Although protons may serve as the charge-carrier ions in aqueous systems (pH values in Table S4),[37] a strong variation in capacities based on Li^+, Na^+, and Mg^{2+} electrolytes (*vide supra*) does not rule out a role for cations during intercalation (Figure 2b). Taken together, it is likely that protons and cations both participate in the intercalation process and influence changes in interlayer spacing (Figure 2c). Moreover, prior reports on intercalation in 2D van der Waals materials describe that, in addition to the intercalating cations themselves, both the nature of cation solvation and the solvent-electrode interactions also influence the interlayer spacing.[24,25,38,39] Overall, a notable expansion of the lattice under polarization, albeit incommensurate with cation size, suggests collective intercalation of both cations and protons in Ni_6HHTT_3.

Electrode kinetics of Ni_3HHTT_2 and Ni_6HHTT_3 were studied using scan rate versus peak current analysis and potentiostatic electrochemical impedance spectroscopy (Figure 3). Nyquist plots display similarly resistive responses in the semicircle, 45° Warburg diffusion, and the vertical capacitive regions for both MOFs. Analyzing the data from CVs recorded over a range of scan rates from 1 to 20 mV/s (Figures S9 & S10) using a power law relation (eq 1, where i is the measured peak current at a given potential, v is the scan rate, and a and b are adjustable parameters) found b values of 0.84 and 0.78 for eclipsed and staggered Ni-MOFs, respectively (inset, Figure 3).

https://doi.org/10.1021/acsenergylett.4c00544
ACS Energy Lett. 2024, 9, 1572−1580

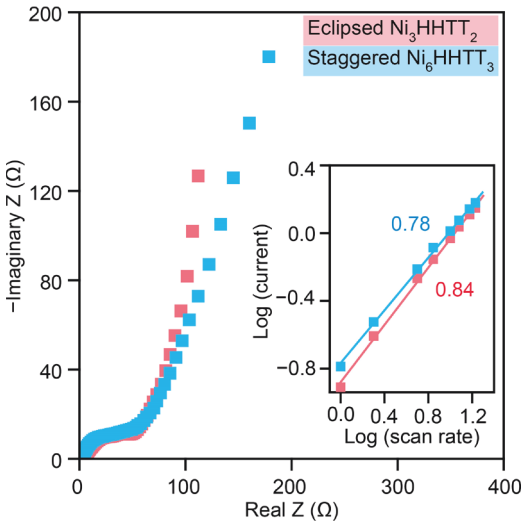

Figure 3. Nyquist plots of potentiostatic electrochemical impedance for Ni_3HHTT_2 and Ni_6HHTT_3 under negative polarization of −0.4 V vs Ag/AgCl in aqueous $NaClO_4$ electrolyte. Frequencies ranging from 10 mHz to 200 kHz are used. (inset) Power-law analysis and *b* values of 0.78 and 0.84 for eclipsed and staggered Ni-MOFs, respectively.

$$i(v) = av^b \quad (1)$$

Taken together, similarly resistive behavior and rapid electrode kinetics between both materials, despite their different ion sorption mechanisms, support a role for protons as charge carrier ions in overall ion sorption of both MOFs. Moreover, the *b* values noted here, which are close to unity, indicate that the redox processes in both materials are not limited by semi-infinite diffusion and can be characterized as pseudocapacitive processes.[40] Whereas reports of pseudocapacitance in MOFs are now increasingly common,[14−17] intercalation-driven pseudocapacitance in an MOF with honeycomb-like sheets is rare.

Ligand-Centered Redox Activity. Electrochemical studies in nonaqueous electrolytes revealed distinct redox behaviors for Ni_3HHTT_2 and Ni_6HHTT_3 in both $LiClO_4$ and $NaClO_4$/acetonitrile (ACN) electrolytes. Ni_6HHTT_3 displayed two distinct sets of reversible redox peaks at −0.18 and −0.42 V vs Ag/AgCl in CVs recorded at a scan rate of 2 mV/s (Figure 4a). Similar sets of two redox peaks were also observed in other nonaqueous electrolytes of propylene carbonate and dimethylformamide (Figure S11a). Moreover, a closer look at CVs in aqueous electrolytes recorded at 0.2 mV/s also identifies two closely placed redox peaks in Ni_6HHTT_3 (Figure S11b). In contrast, only one set of peaks was observed for eclipsed Ni_3HHTT_2 (Figure 4a). Overall, while the difference in the number of redox peaks for both MOFs is the subject for the next section, the origin of redox behavior itself as either a metal- and/or ligand-based process is evaluated using *ex situ* X-

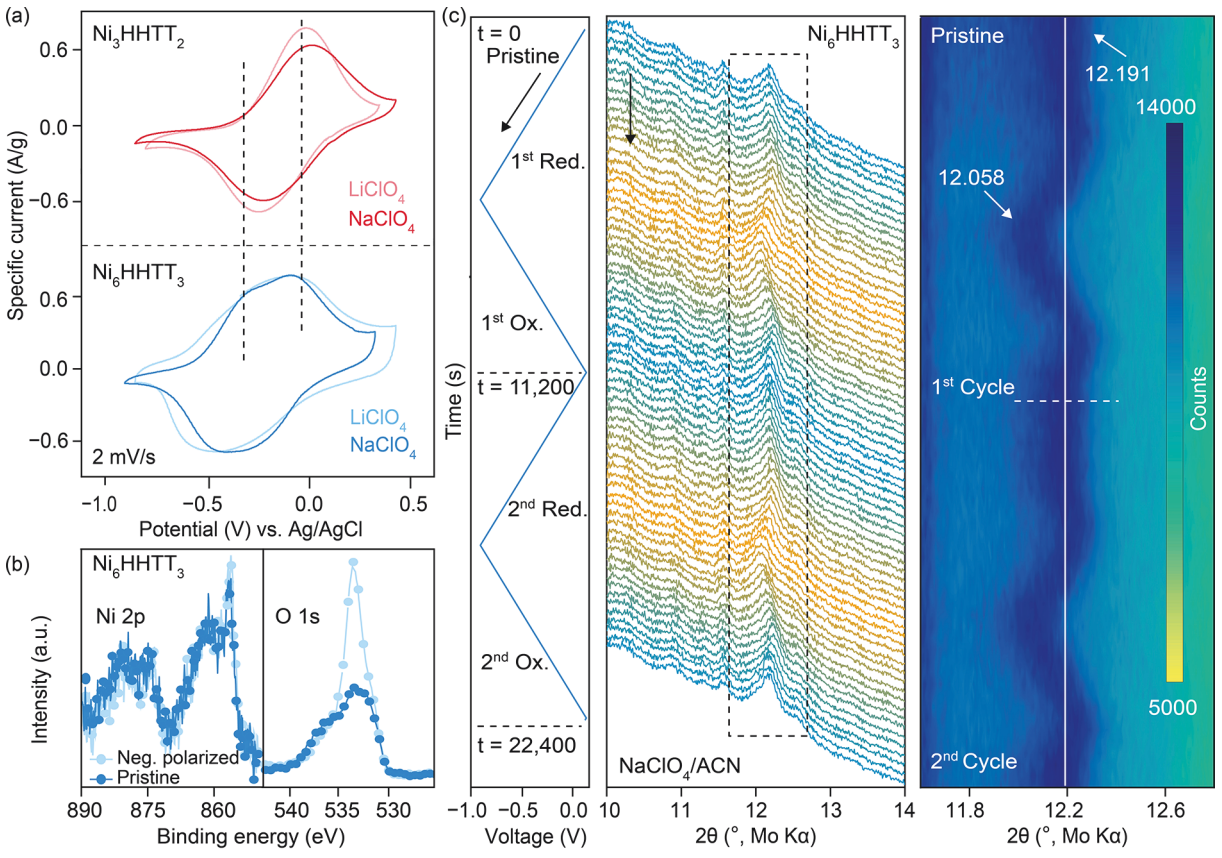

Figure 4. (a) Cyclic voltammetry curves of Ni_3HHTT_2 and Ni_6HHTT_3 at a scan rate of 2 mV/s using $LiClO_4$ $NaClO_4$ in nonaqueous solvents (Acetonitrile - ACN). (b) High-resolution X-ray photoelectron spectra of Ni 2p and O 1s of pristine and negatively polarized Ni_6HHTT_3. (c) *In situ* PXRD patterns Mo K alpha (0.71 Å) of Ni_6HHTT_3 in $NaClO_4$/ACN during two cycles of cyclic voltammetry scans at 0.2 mV/s. Reversible shifts in the reflections corresponding to interlayer spacing of Ni_6HHTT_3 are noted. The right-side panel shows a contour plot that highlights these reversible changes.

https://doi.org/10.1021/acsenergylett.4c00544
ACS Energy Lett. 2024, 9, 1572−1580

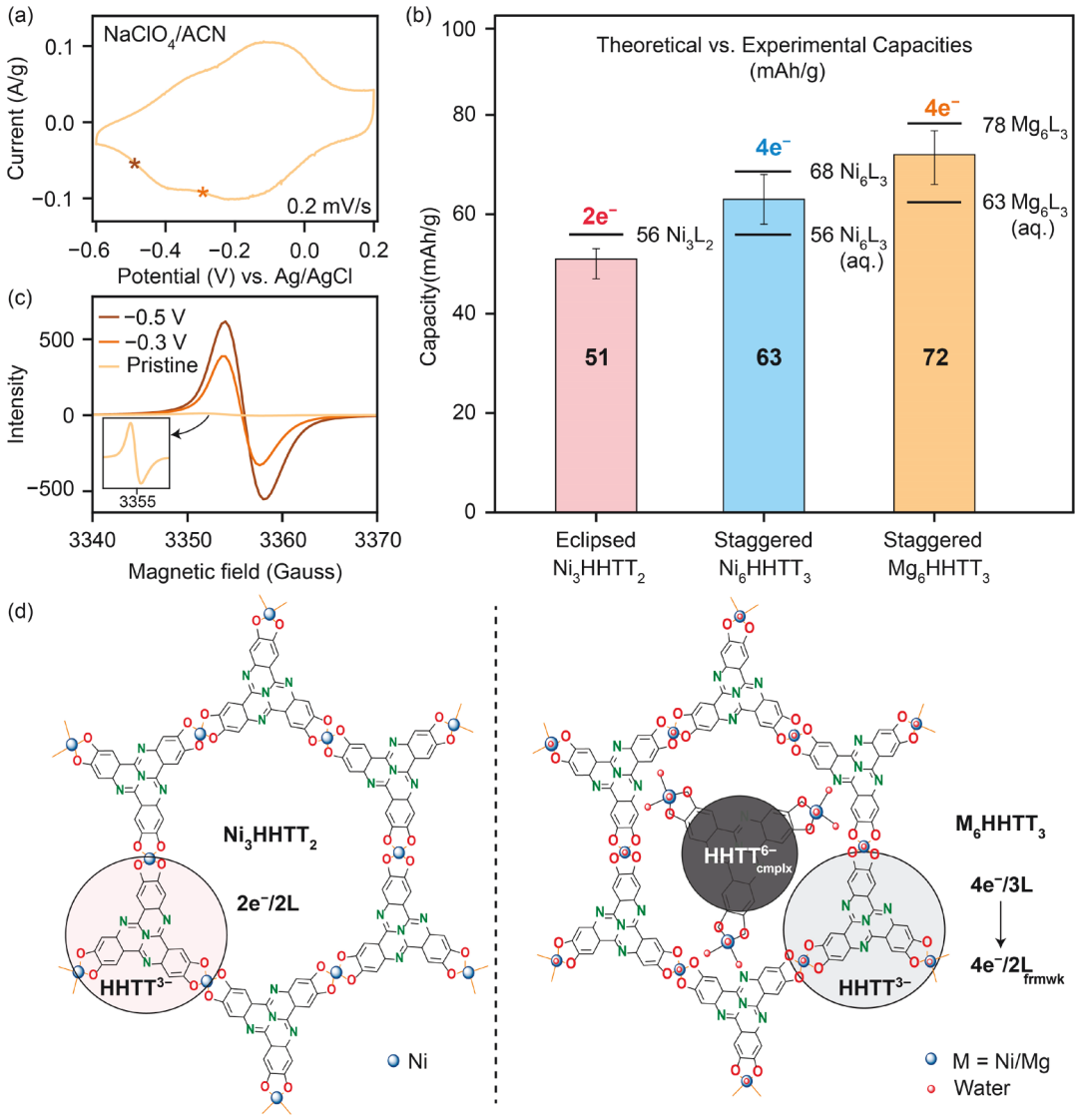

Figure 5. (a) Cyclic voltammetry curve of Mg_6HHTT_3 at a scan rate of 0.2 mV/s using $NaClO_4$ in acetonitrile (ACN). (b) Theoretical and maximum experimental specific capacity values of M_6HHTT_3 (M = Ni/Mg) and Ni_3HHTT_2. Experimental capacity of Ni_3HHTT_2 matches a calculated $2e^-$ process for a formula unit of M_3L_2 (L = HHTT). Experimental capacities of M_6HHTT_3 fall within a range of capacities calculated for a $4e^-$ process for M_6L_3 and its hydrous structure $-M_6L_3{\cdot}18H_2O$ (indicated as aqueous). (c) Electron paramagnetic resonance spectra of pristine and negatively polarized (−0.3 V and −0.5 V vs Ag/AgCl) of Mg_6HHTT_3 in $NaClO_4$/ACN. (inset) Zoomed response of the pristine electrode. (d) Mechanism of charge storage in Ni_3HHTT_2 and M_6HHTT_3 (M = Ni/Mg). While Ni_3HHTT_2 undergoes a $2e^-/2L$ reduction, both M_6HHTT_3 MOFs undergo $4e^-/3L$ processes and, due to the redox innocence of the inserted complex, undergo $4e^-/2L$ in the framework. Circles are drawn to highlight L_{cmplx} and L_{frmwk} for the reader.

ray photoelectron spectra (XPS) of polarized samples (Figures 4b, S12, & S13).[41] High-resolution XPS data of Ni 2p in both MOFs essentially remain unchanged relative to the pristine MOFs. On the other hand, pronounced enhancement of the component at 533 eV for O 1s in both MOFs indicated enhanced single bond character of C═O under negative polarization, in line with a ligand-centered reduction process in both MOFs. Similar ligand-centered redox processes are reported for several Ni-based 2D MOFs and coordination polymers.[8,14,15,24,38]

Ex situ PXRD analyses were performed on both MOFs in $NaClO_4$/(ACN) to evaluate intercalation and compare with prior analyses in aqueous systems. First, similar to the observations in aqueous systems, Ni_6HHTT_3 displayed an expanded lattice upon polarization, whereas no notable shifts in the XRD patterns were noted for Ni_3HHTT_2 (Figures S14 & S15). Notably, the extent of lattice expansion in Ni_6HHTT_3 here is greater than in aqueous electrolytes (Figure S14 & Table S3), suggesting an enhanced role for sodium cations as charge-carriers in ACN, relative to protons in aqueous solutions. Additional *in situ* PXRD studies were then performed on Ni_6HHTT_3 in $NaClO_4$/ACN to probe the reversibility of the lattice expansion noted under the *ex situ* conditions (Figures 4c, S16, & S17). Scanning Ni_6HHTT_3 under a negative bias from 0.23 to −0.90 V in $NaClO_4$/ACN caused a gradual decrease in the 2θ angle of reflection at 12.191 to ∼12.058°, indicating a gradual expansion of the lattice (Figure 4c). Reverse scanning under positive bias caused systematic reversal of the lattice expansion leading to its original state. Moreover, diffraction patterns in the second CV cycle mirror the behavior observed in the first cycle, confirming the complete reversibility of structural changes in Ni_6HHTT_3

https://doi.org/10.1021/acsenergylett.4c00544
ACS Energy Lett. 2024, 9, 1572−1580

under external bias. For the sake of completeness, the reversibility of lattice expansion was also probed and observed in *ex situ* PXRD analyses (Figures S18), validating the ex situ PXRD procedures used in this work. Overall, the reversible expansion of the lattice during cycling confirms an intercalation-based charge storage mechanism in Ni_6HHTT_3 and differentiates with the pore-base sorption in Ni_3HHTT_2. Furthermore, a comparison of EIS under negative polarization in $NaClO_4$/ACN finds greater resistance for charge transfer in Ni_6HHTT_3 than in Ni_3HHTT_2 (Figure S19), indicating intercalation as a more resistive process than in-pore sorption.

The observation of ligand-centered redox mechanisms was further evaluated by synthesizing and studying an analogous staggered Mg_6HHTT_3 that has redox-innocent metal ions. CVs recorded for Mg_6HHTT_3 at 0.2 mV/s in 0.5 M $NaClO_4$/ACN display two sets of distinct redox peaks, similar to Ni_6HHTT_3 (Figure 5a), with an even higher specific capacity of 72 ± 4 mAh/g (Figure 5b). *Ex situ* PXRD patterns of Mg_6HHTT_3 (Figure S20, Table S3) confirm intercalation and expansion of layers, and Mg 2p and O 1s XPS data support a ligand-centered process (Figure S21). Given the diamagnetic nature of Mg^{2+}, Mg_6HHTT_3 is also more suitable than Ni_6HHTT_3 for electron paramagnetic resonance (EPR) measurements to investigate the ligand-centered redox processes. EPR analyses were performed at room temperature on pristine and polarized Mg_6HHTT_3 samples (details in experimental methods) to gain deeper insights into the redox behavior (Figures 5c, S22). Pristine Mg_6HHTT_3 displayed a sharp signal with g = 2.04, agreeing well with the typical signal for organic radical with S = 1/2, which supports assignment of the HHTT in framework to have a formal charge state of −3 in Mg_6HHTT_3.[19] Additionally, the absence of other signals in the spectrum agrees with the close-shell nature of Mg^{2+} (Figure S22a).[42] Quantitative assessment of the organic radical using TEMPO (2,2,6,6-tetramethylpiperidine 1-oxyl)/KBr standards[42,43] found 0.86−1.19 radicals per unit HHTT, further confirming the assignment of HHTT formal charge state as −3 (Figures 5d & S22b, Tables S5 & S6). Increasingly greater EPR intensities were observed for samples polarized at increasingly negative potentials of −0.3 and −0.5 V vs Ag/AgCl corresponding to first and second reduction events in the CVs (Figure 5a). These observations, taken together with XPS data, confirm that both redox events in nonporous M_6HHTT_3 originate from ligand redox activity. A recent report on Mn-based MOFs indicated the possibility of metal mediation in a ligand-centered reversible oxidation.[44] In our case, transient reduction of the metal nodes, particularly of Mg^{2+}, is unlikely in the chosen potential window. Although ex situ EPR analyses on Ni_6HHTT_3 showed no signals from a Ni^+ species upon reduction (Figure S25), further studies are necessary to confirm or dispute metal mediation in the overall ligand reduction.

Experimental Versus Theoretical Capacities. Experimental capacities and calculated values were compared to understand the distinct one- versus two-ligand-centered redox events between the eclipsed and staggered MOFs, respectively (Table S7). Eclipsed Ni-MOF, with a formula of Ni_3L_2 (L = HHTT), has a theoretical capacity of 56 mAh/g for a two-electron process (Figure 5b). CVs at the slowest scan rates in aqueous electrolytes delivered maximum capacities of 50−54 mAh/g, confirming a two-electron process per two ligands ($2e^-/2L$) in Ni_3L_2 or $1e^-/1L$. This $1e^-/1L$ process matches well with the single redox event observed for Ni_3L_2 in its CVs. On the other hand, a similar two-electron redox process for nonporous Ni-MOF, with a formula of $Ni_6L_3{\cdot}18H_2O$, has a theoretical capacity of only 23 mAh/g, or 34 mAh/g in its anhydrous form of Ni_6L_3. However, experimental capacities of nonporous Ni-MOF were consistently higher in the range of 63−68 mAh/g (Figure 5b) for nonaqueous electrolytes and around 50 mAh/g in aqueous electrolytes. Instead, the experimental values match the theoretical capacities calculated for a four-electron process. Control studies were performed by testing Ni_6L_3 in a variety of electrode compositions that had 60−100% active material content and on various substrates including on carbon fiber paper, as a slurry coated on stainless steel disks, and as free-standing films. All electrode configurations delivered similarly high capacities of ∼58−63 mAh/g at 0.5 mV/s, confirming that electrode compositions and preparation conditions do not affect the discussion here (Figures S23 & S24). Similarly, experimental capacities of nonporous Mg-MOF also match a four-electron process with theoretical capacities of 78 and 63 mAh/g for hydrated and anhydrous Mg_6L_3, respectively (Figure 5b). Taken together, both staggered MOFs (Ni and Mg) undergo four-electron reduction per three ligands ($4e^-/3L$) in M_6L_3 (M = Ni^{2+} or Mg^{2+}). This interesting $4e^-/3L$ process raises further questions on how the $4e^-$ ions are distributed between the 3L in M_6L_3 and how they explain the two redox events observed in CVs.

Framework Versus Cluster Redox Activity. Hexa-substituted aromatic ligands in catecholate- and amine-based MOFs are reported to exhibit reduction from their pristine charge state of −3 to a maximum of −6.[29,45,46] In the case of Ni_3L_2, the observation of one redox event and $1e^-/1L$ storage capacities together support the reversible reduction of HHTT from its pristine formal charge of −3 to a reduced state of −4. The case for nonporous M_6L_3 (M = Ni or Mg) MOFs is relatively complex. They show two distinct events in CVs, store four electrons, and have two types of HHTT ligands: one L in the trinuclear complex (L_{cmplx}) and two Ls in the framework (L_{frmwk}). The formal charge state of L_{frmwk} is found to be −3 based on bond length measurements (Table S8) and EPR analysis, rendering them available for reduction. On the other hand, the charge state of L_{cmplx} was assigned as −6 (its maximum reduced state) based on the evidence from elemental analyses[19] and charge balance arguments with three M^{2+} ions,[29] indicating its innocence toward further reduction. Taken together, these arguments indicate that the $4e^-/3L$ reduction of M_6L_3 occurs entirely on the two framework ligands, making it a $4e^-/2L_{frmwk}$ or $2e^-/1L_{frmwk}$ process (Figure S26). Interestingly, continuous cycling of CVs in Ni_6L_3 evolves the two redox peaks into equal events with similar currents (Figure S27), supporting the proposed 2-step, $2e^-/1L_{frmwk}$ reduction. Additionally, both of these peaks occur at potentials different from the response noted for a solution state CV of HHTT ligand, confirming that the observed reductions are related to the MOFs and not to ligand residues (Figure S27). Overall, the $2e^-/1L_{frmwk}$ reduction in staggered M_6L_3 is 2-fold higher than the $1e^-/1L_{frmwk}$ reduction observed for eclipsed Ni_3L_2. This strong modulation in a ligand's redox behavior between comparable 2D MOFs is the first such observation. While further investigations into the factors behind this modulation are necessary, the differences in packing motifs and the resulting band structures provide preliminary clues.[47] The eclipsed phase of Ni_3L_2 has widely dispersed bands consisting of orbitals from both metal ions and ligands at the Fermi level.[19] In contrast, the staggered phase of

https://doi.org/10.1021/acsenergylett.4c00544
ACS Energy Lett. 2024, 9, 1572−1580

M_6L_3 MOFs have ineffective orbital mixing and narrow bands that are centered on the framework ligands.[19] Together, the framework ligands in both MOFs exist in different electron delocalization environments and differ in their electron uptake during electrochemical reduction, despite both existing in a formal charge state of −3.

The prospect of intercalation-based charge storage in staggered, nonporous MOFs is evaluated in a family of HHTT-based 2D MOFs. Nonporous MOFs are formed with HHTT linker when Ni^{2+} and Mg^{2+} metal nodes adapt octahedral coordination geometry, engage in staggered packing of 2D sheets, and impose guest complex interpenetration into the honeycomb-like sheets of M_6HHTT_3 (M = Ni^{2+} and Mg^{2+}). A prototypical, porous 2D Ni_3HHTT_2 with honeycomb-like sheets is formed when Ni^{2+} adapts square-planar geometry and the layers arrange in an eclipsed fashion. Together, this set of MOFs served as an ideal family to evaluate electrochemical behavior and investigate underlying redox behaviors. Electrochemical studies and ex situ characterization in a range of aqueous and nonaqueous electrolytes found intercalation-based charge storage behavior in both staggered M_6HHTT_3 MOFs and a typical pore-based charge storage in the eclipsed Ni_3HHTT_2. Mg_6HHTT_3 delivered the highest specific capacity of 78 mAh/g, greater than its porous counterpart, presenting an important motivation for future exploration of nonporous MOFs. Investigation of the redox behavior found that, despite undergoing ligand-centered redox processes, eclipsed and staggered MOFs differ by storing two and four electrons per formula unit, respectively. This modulation in redox activity is correlated to distinct structural packing motifs and their electronic delocalization.

■ ASSOCIATED CONTENT

Supporting Information

The Supporting Information is available free of charge at https://pubs.acs.org/doi/10.1021/acsenergylett.4c00544.

Experimental methods; synthetic procedures; ex situ characterization procedures; electrochemical test procedures, cyclic voltammetry data; X-ray photoelectron spectra; powder X-ray diffraction data; electron paramagnetic resonance data; and quantification (PDF)

■ AUTHOR INFORMATION

Corresponding Author

Harish Banda − *Department of Chemistry and Biochemistry, The University of Texas at El Paso, El Paso 79968 Texas, United States;* orcid.org/0000-0002-1630-4450; Email: hbanda1@utep.edu

Authors

Satya Prakash Suman − *Department of Chemistry and Biochemistry, The University of Texas at El Paso, El Paso 79968 Texas, United States*

Gopi M. R. Dontireddy − *Department of Chemistry and Biochemistry, The University of Texas at El Paso, El Paso 79968 Texas, United States*

Tianyang Chen − *Department of Chemical Engineering, Stanford University, Stanford 94305 California, United States;* orcid.org/0000-0003-3142-8176

Jiande Wang − *Department of Chemistry, Massachusetts Institute of Technology, Cambridge 02139 Massachusetts, United States*

Jin-Hu Dou − *School of Materials Science and Engineering, Peking University, Beijing 100871, China;* orcid.org/0000-0002-6920-9051

Complete contact information is available at: https://pubs.acs.org/10.1021/acsenergylett.4c00544

Notes

The authors declare no competing financial interest.

■ ACKNOWLEDGMENTS

The authors acknowledge access to the core instrumentation facilities provided by the Department of Chemistry and Biochemistry at the University of Texas, El Paso (UTEP). Authors thank Dr. Sohan De Silva and Dr. Alejandro Metta for their support and discussions. This work used the X-ray photoelectron spectrometer at UTEP funded by the National Science Foundation MRI program under Award No. NSF 2216473. The authors acknowledge Massachusetts Institute of Technology, Department of Chemistry Instrumentation Facility, and MRSEC. This work is supported by the startup grant provided to H.B. by the University of Texas at El Paso and the Rising Star Award granted to H.B. by the University of Texas system.

■ REFERENCES

(1) Xie, L. S.; Skorupskii, G.; Dincă, M. Electrically Conductive Metal−Organic Frameworks. *Chem. Rev.* **2020**, *120* (16), 8536−8580.

(2) Yu, M.; Dong, R.; Feng, X. Two-Dimensional Carbon-Rich Conjugated Frameworks for Electrochemical Energy Applications. *J. Am. Chem. Soc.* **2020**, *142* (30), 12903−12915.

(3) Ko, M.; Mendecki, L.; Mirica, K. A. Conductive Two-Dimensional Metal−Organic Frameworks as Multifunctional Materials. *Chem. Commun.* **2018**, *54* (57), 7873−7891.

(4) Liu, J.; Zhou, Y.; Xie, Z.; Li, Y.; Liu, Y.; Sun, J.; Ma, Y.; Terasaki, O.; Chen, L. Conjugated Copper−Catecholate Framework Electrodes for Efficient Energy Storage. *Angew. Chem.* **2020**, *59* (3), 1081−1086.

(5) Shin, S.-J.; Gittins, J. W.; Balhatchet, C. J.; Walsh, A.; Forse, A. C. Metal−Organic Framework Supercapacitors: Challenges and Opportunities. *Adv. Funct. Mater.* **2023**, No. 2308497.

(6) Hong, C. N.; Crom, A. B.; Feldblyum, J. I.; Lukatskaya, M. R. Metal-Organic Frameworks for Fast Electrochemical Energy Storage: Mechanisms and Opportunities. *Chem.* **2023**, *9* (4), 798−822.

(7) Bi, S.; Banda, H.; Chen, M.; Niu, L.; Chen, M.; Wu, T.; Wang, J.; Wang, R.; Feng, J.; Chen, T.; Dincă, M.; Kornyshev, A. A.; Feng, G. Molecular Understanding of Charge Storage and Charging Dynamics in Supercapacitors with MOF Electrodes and Ionic Liquid Electrolytes. *Nat. Mater.* **2020**, *19* (5), 552−558.

(8) Sheberla, D.; Bachman, J. C.; Elias, J. S.; Sun, C.-J.; Shao-Horn, Y.; Dincă, M. Conductive MOF Electrodes for Stable Supercapacitors with High Areal Capacitance. *Nat. Mater.* **2017**, *16* (2), 220−224.

(9) Sheberla, D.; Sun, L.; Blood-Forsythe, M. A.; Er, S.; Wade, C. R.; Brozek, C. K.; Aspuru-Guzik, A.; Dincă, M. High Electrical Conductivity in Ni_3(2,3,6,7,10,11-Hexaiminotriphenylene)$_2$, a Semiconducting Metal−Organic Graphene Analogue. *J. Am. Chem. Soc.* **2014**, *136* (25), 8859−8862.

(10) Gittins, J. W.; Balhatchet, C. J.; Chen, Y.; Liu, C.; Madden, D. G.; Britto, S.; Golomb, M. J.; Walsh, A.; Fairen-Jimenez, D.; Dutton, S. E.; Forse, A. C. Insights into the Electric Double-Layer Capacitance of Two-Dimensional Electrically Conductive Metal−Organic Frameworks. *J. Mater. Chem. A* **2021**, *9* (29), 16006−16015.

(11) Shin, S.-J.; Gittins, J. W.; Golomb, M. J.; Forse, A. C.; Walsh, A. Microscopic Origin of Electrochemical Capacitance in Metal−Organic Frameworks. *J. Am. Chem. Soc.* **2023**, *145* (26), 14529−14538.

(12) Wrogemann, J. M.; Lüther, M. J.; Bärmann, P.; Lounasvuori, M.; Javed, A.; Tiemann, M.; Golnak, R.; Xiao, J.; Petit, T.; Placke, T.;

Winter, M. Overcoming Diffusion Limitation of Faradaic Processes: Property-Performance Relationships of 2D Conductive Metal-Organic Framework Cu3(HHTP)2 for Reversible Lithium-Ion Storage. *Angew. Chem.* **2023**, *62* (26), No. e202303111.
(13) Park, J.; Lee, M.; Feng, D.; Huang, Z.; Hinckley, A. C.; Yakovenko, A.; Zou, X.; Cui, Y.; Bao, Z. Stabilization of Hexaaminobenzene in a 2D Conductive Metal−Organic Framework for High Power Sodium Storage. *J. Am. Chem. Soc.* **2018**, *140* (32), 10315−10323.
(14) Feng, D.; Lei, T.; Lukatskaya, M. R.; Park, J.; Huang, Z.; Lee, M.; Shaw, L.; Chen, S.; Yakovenko, A. A.; Kulkarni, A.; Xiao, J.; Fredrickson, K.; Tok, J. B.; Zou, X.; Cui, Y.; Bao, Z. Robust and Conductive Two-Dimensional Metal−organic Frameworks with Exceptionally High Volumetric and Areal Capacitance. *Nat. Energy* **2018**, *3* (1), 30−36.
(15) Lukatskaya, M. R.; Feng, D.; Bak, S.-M.; To, J. W. F.; Yang, X.-Q.; Cui, Y.; Feldblyum, J. I.; Bao, Z. Understanding the Mechanism of High Capacitance in Nickel Hexaaminobenzene-Based Conductive Metal−Organic Frameworks in Aqueous Electrolytes. *ACS Nano* **2020**, *14* (11), 15919−15925.
(16) Zhang, P.; Wang, M.; Liu, Y.; Fu, Y.; Gao, M.; Wang, G.; Wang, F.; Wang, Z.; Chen, G.; Yang, S.; Liu, Y.; Dong, R.; Yu, M.; Lu, X.; Feng, X. Largely Pseudocapacitive Two-Dimensional Conjugated Metal−Organic Framework Anodes with Lowest Unoccupied Molecular Orbital Localized in Nickel-Bis(Dithiolene) Linkages. *J. Am. Chem. Soc.* **2023**, *145* (11), 6247−6256.
(17) Zhang, P.; Wang, M.; Liu, Y.; Yang, S.; Wang, F.; Li, Y.; Chen, G.; Li, Z.; Wang, G.; Zhu, M.; Dong, R.; Yu, M.; Schmidt, O. G.; Feng, X. Dual-Redox-Sites Enable Two-Dimensional Conjugated Metal−Organic Frameworks with Large Pseudocapacitance and Wide Potential Window. *J. Am. Chem. Soc.* **2021**, *143* (27), 10168−10176.
(18) Liu, J.; Song, X.; Zhang, T.; Liu, S.; Wen, H.; Chen, L. 2D Conductive Metal−Organic Frameworks: An Emerging Platform for Electrochemical Energy Storage. *Angew. Chem.* **2021**, *60* (11), 5612−5624.
(19) Dou, J.-H.; Arguilla, M. Q.; Luo, Y.; Li, J.; Zhang, W.; Sun, L.; Mancuso, J. L.; Yang, L.; Chen, T.; Parent, L. R.; Skorupskii, G.; Libretto, N. J.; Sun, C.; Yang, M. C.; Dip, P. V.; Brignole, E. J.; Miller, J. T.; Kong, J.; Hendon, C. H.; Sun, J.; Dincă, M. Atomically Precise Single-Crystal Structures of Electrically Conducting 2D Metal−Organic Frameworks. *Nat. Mater.* **2021**, *20* (2), 222−228.
(20) Maeda, H.; Takada, K.; Fukui, N.; Nagashima, S.; Nishihara, H. Conductive Coordination Nanosheets: Sailing to Electronics, Energy Storage, and Catalysis. *Coord. Chem. Rev.* **2022**, *470*, No. 214693.
(21) Zhang, Y.; Ang, E. H.; Yang, Y.; Ye, M.; Du, W.; Li, C. C. Interlayer Chemistry of Layered Electrode Materials in Energy Storage Devices. *Adv. Funct. Mater.* **2021**, *31* (4), No. 2007358.
(22) Lukatskaya, M. R.; Mashtalir, O.; Ren, C. E.; Dall'Agnese, Y.; Rozier, P.; Taberna, P. L.; Naguib, M.; Simon, P.; Barsoum, M. W.; Gogotsi, Y. Cation Intercalation and High Volumetric Capacitance of Two-Dimensional Titanium Carbide. *Science* **2013**, *341* (6153), 1502−1505.
(23) Novoselov, K. S.; Mishchenko, A.; Carvalho, A.; Castro Neto, A. H. 2D Materials and van Der Waals Heterostructures. *Science* **2016**, *353* (6298), No. aac9439.
(24) Banda, H.; Dou, J.-H.; Chen, T.; Libretto, N. J.; Chaudhary, M.; Bernard, G. M.; Miller, J. T.; Michaelis, V. K.; Dincă, M. High-Capacitance Pseudocapacitors from Li+ Ion Intercalation in Nonporous, Electrically Conductive 2D Coordination Polymers. *J. Am. Chem. Soc.* **2021**, *143* (5), 2285−2292.
(25) Banda, H.; Dou, J.-H.; Chen, T.; Zhang, Y.; Dincă, M. Dual-Ion Intercalation and High Volumetric Capacitance in a Two-Dimensional Non-Porous Coordination Polymer. *Angew.e Chem.* **2021**, *133* (52), 27325−27331.
(26) Simon, P.; Gogotsi, Y. Perspectives for Electrochemical Capacitors and Related Devices. *Nat. Mater.* **2020**, *19* (11), 1151−1163.
(27) Kawaguchi, N.; Shibata, K.; Mizoguchi, T. Possible New Graphite Intercalation Compounds for Superconductors and Charge Density Wave Materials: Systematic Simulations with Various Intercalants Using a van Der Waals Density Functional Method. *J. Phys. Chem. C* **2023**, *127* (20), 9833−9843.
(28) Jung, Y.; Zhou, Y.; Cha, J. J. Intercalation in Two-Dimensional Transition Metal Chalcogenides. *Inorg. Chem. Front.* **2016**, *3* (4), 452−463.
(29) Hmadeh, M.; Lu, Z.; Liu, Z.; Gándara, F.; Furukawa, H.; Wan, S.; Augustyn, V.; Chang, R.; Liao, L.; Zhou, F.; Perre, E.; Ozolins, V.; Suenaga, K.; Duan, X.; Dunn, B.; Yamamto, Y.; Terasaki, O.; Yaghi, O. M. New Porous Crystals of Extended Metal-Catecholates. *Chem. Mater.* **2012**, *24* (18), 3511−3513.
(30) Banda, H.; Daffos, B.; Périé, S.; Chenavier, Y.; Dubois, L.; Aradilla, D.; Pouget, S.; Simon, P.; Crosnier, O.; Taberna, P.-L.; Duclairoir, F. Ion Sieving Effects in Chemically Tuned Pillared Graphene Materials for Electrochemical Capacitors. *Chem. Mater.* **2018**, *30* (9), 3040−3047.
(31) Banda, H.; Périé, S.; Daffos, B.; Taberna, P.-L.; Dubois, L.; Crosnier, O.; Simon, P.; Lee, D.; De Paëpe, G.; Duclairoir, F. Sparsely Pillared Graphene Materials for High-Performance Supercapacitors: Improving Ion Transport and Storage Capacity. *ACS Nano* **2019**, *13* (2), 1443−1453.
(32) Boyd, S.; Ganeshan, K.; Tsai, W.-Y.; Wu, T.; Saeed, S.; Jiang, D.; Balke, N.; van Duin, A. C. T.; Augustyn, V. Effects of Interlayer Confinement and Hydration on Capacitive Charge Storage in Birnessite. *Nat. Mater.* **2021**, *20* (12), 1689−1694.
(33) Kim, J. W.; Augustyn, V.; Dunn, B. The Effect of Crystallinity on the Rapid Pseudocapacitive Response of Nb2O5. *Adv. Energy Mater.* **2012**, *2* (1), 141−148.
(34) Augustyn, V.; Come, J.; Lowe, M. A.; Kim, J. W.; Taberna, P.-L.; Tolbert, S. H.; Abruña, H. D.; Simon, P.; Dunn, B. High-Rate Electrochemical Energy Storage through Li+ Intercalation Pseudocapacitance. *Nat. Mater.* **2013**, *12* (6), 518−522.
(35) Segalini, J.; Iwama, E.; Taberna, P.-L.; Gogotsi, Y.; Simon, P. Steric Effects in Adsorption of Ions from Mixed Electrolytes into Microporous Carbon. *Electrochem. Commun.* **2012**, *15* (1), 63−65.
(36) Park, M. J.; Yaghoobnejad Asl, H.; Manthiram, A. Multivalent-Ion versus Proton Insertion into Battery Electrodes. *ACS Energy Lett.* **2020**, *5* (7), 2367−2375.
(37) Cheng, S.; Cao, Z.; Liu, Y.; Zhang, J.; Cavallo, L.; Xie, E.; Fu, J. Ballistic Electrolyte Ion Transport with Undisturbed Pathways for Ultrahigh-Rate Electrochemical Energy Storage Devices. *Energy Environ. Sci.* **2024**, *17*, 1997.
(38) Wu, Z.; Adekoya, D.; Huang, X.; Kiefel, M. J.; Xie, J.; Xu, W.; Zhang, Q.; Zhu, D.; Zhang, S. Highly Conductive Two-Dimensional Metal−Organic Frameworks for Resilient Lithium Storage with Superb Rate Capability. *ACS Nano* **2020**, *14* (9), 12016−12026.
(39) Wang, X.; Mathis, T. S.; Li, K.; Lin, Z.; Vlcek, L.; Torita, T.; Osti, N. C.; Hatter, C.; Urbankowski, P.; Sarycheva, A.; Tyagi, M.; Mamontov, E.; Simon, P.; Gogotsi, Y. Influences from Solvents on Charge Storage in Titanium Carbide MXenes. *Nat. Energy* **2019**, *4* (3), 241−248.
(40) Augustyn, V.; Simon, P.; Dunn, B. Pseudocapacitive Oxide Materials for High-Rate Electrochemical Energy Storage. *Energy Environ. Sci.* **2014**, *7* (5), 1597−1614.
(41) Amores, M.; Wada, K.; Sakaushi, K.; Nishihara, H. Reversible Energy Storage in Layered Copper-Based Coordination Polymers: Unveiling the Influence of the Ligand's Functional Group on Their Electrochemical Properties. *J. Phys. Chem. C* **2020**, *124* (17), 9215−9224.
(42) Sun, L.; Yang, L.; Dou, J.-H.; Li, J.; Skorupskii, G.; Mardini, M.; Tan, K. O.; Chen, T.; Sun, C.; Oppenheim, J. J.; Griffin, R. G.; Dincă, M.; Rajh, T. Room-Temperature Quantitative Quantum Sensing of Lithium Ions with a Radical-Embedded Metal−Organic Framework. *J. Am. Chem. Soc.* **2022**, *144* (41), 19008−19016.
(43) Chen, Q.; Adeniran, O.; Liu, Z.-F.; Zhang, Z.; Awaga, K. Graphite-like Charge Storage Mechanism in a 2D π−d Conjugated Metal−Organic Framework Revealed by Stepwise Magnetic Monitoring. *J. Am. Chem. Soc.* **2023**, *145* (2), 1062−1071.

https://doi.org/10.1021/acsenergylett.4c00544
ACS Energy Lett. 2024, 9, 1572−1580

(44) Rambabu, D.; Lakraychi, A. E.; Wang, J.; Sieuw, L.; Gupta, D.; Apostol, P.; Chanteux, G.; Goossens, T.; Robeyns, K.; Vlad, A. An Electrically Conducting Li-Ion Metal−Organic Framework. *J. Am. Chem. Soc.* **2021**, *143* (30), 11641−11650.
(45) Yang, L.; He, X.; Dincă, M. Triphenylene-Bridged Trinuclear Complexes of Cu: Models for Spin Interactions in Two-Dimensional Electrically Conductive Metal−Organic Frameworks. *J. Am. Chem. Soc.* **2019**, *141* (26), 10475−10480.
(46) Yang, L.; Dincă, M. Redox Ladder of Ni_3 Complexes with Closed-Shell, Mono-, and Diradical Triphenylene Units: Molecular Models for Conductive 2D MOFs. *Angew. Chem.* **2021**, *60* (44), 23784−23789.
(47) Dong, R.; Han, P.; Arora, H.; Ballabio, M.; Karakus, M.; Zhang, Z.; Shekhar, C.; Adler, P.; Petkov, P. S.; Erbe, A.; Mannsfeld, S. C. B.; Felser, C.; Heine, T.; Bonn, M.; Feng, X.; Cánovas, E. High-Mobility Band-like Charge Transport in a Semiconducting Two-Dimensional Metal−Organic Framework. *Nat. Mater.* **2018**, *17* (11), 1027−1032.

https://doi.org/10.1021/acsenergylett.4c00544
ACS Energy Lett. 2024, 9, 1572−1580